第 49 卷 第 1 期/2022 年 1 月/中国激光 研究论文

中国激光

全正色散双包层拉锥 Ge-As-Se-Te 光纤中的宽带相干超连续谱产生

王莹莹[1]，张楠[2]，张培晴[1,3,4,5]，王训四[1,3,4,5]，戴世勋[1,3,4,5*]

[1]宁波大学高等技术研究院红外材料及器件实验室，浙江 宁波 315211；

[2]南京大学电子科学与工程学院，江苏 南京 210093；

[3]浙江省光电探测材料及器件重点实验室，浙江 宁波 315211；

[4]先进红外光电材料及器件浙江省工程研究中心，浙江 宁波 315211；

[5]红外材料及器件研究浙江国际科技合作基地，浙江 宁波 315211

摘要 制备了具有全正色散特性的 Ge-As-Se-Te 双包层拉锥光纤，并研究了其中的红外超连续谱输出特性。所采用的拉锥光纤的纤芯直径为 12 μm，外包层直径为 108 μm，锥区长度为 9.8 mm。利用 6 μm 的飞秒激光泵浦 10 cm 长的拉锥光纤，获得了 1.5～14.3 μm 的超连续谱输出。与同样纤芯直径的单包层拉锥光纤相比，双包层结构不仅增强了光纤的机械强度，还减少了泵浦能量在锥区的损耗，进一步拓宽了超连续谱的宽度。模拟计算结果表明，该超连续谱具有高的相干性。

关键词 激光光学；非线性光学；光纤制备；超连续谱产生；光纤光学

中图分类号 O437 **文献标志码** A **doi**：10.3788/CJL202249.0101010

1 引 言

中红外超连续谱（supercontinuum，SC）光源具有宽带宽、高亮度以及高相干性等特点，在疾病诊断、食品质量监测以及分子传感等领域具有重要的应用价值[1-4]。目前，已有多种特种玻璃基质材料被用作中红外 SC 产生的非线性介质，包括碲酸盐[5-7]、氟化物[8-9]以及硫系玻璃[10-12]等。其中，硫系玻璃具有更宽的红外透过窗口（可至 20 μm）和更高的光学非线性系数（比石英玻璃高约三个数量级）[11]，因此硫系光纤被认为是获得中红外甚至远红外宽带 SC 输出的理想介质。

为了获得超宽的 SC 输出，一般采用超短脉冲在光纤的反常色散区近零色散点进行泵浦[13-15]。此时 SC 的展宽机制主要是与孤子有关的传输效应，如孤子分裂、孤子自频移等。在调制不稳定性的作用下，产生的 SC 各个频谱成分之间往往具有不确定的相位关系，因此 SC 的相干性较差[16]。光学相干层析成像以及高精密频率测量等应用往往需要非常高的光学分辨率，因此要求 SC 具有较高的相干性[17-18]。

目前，获得高相干性 SC 的方法主要是采用超短脉冲泵浦具有全正色散特性的光纤[19]。在这种情况下，SC 的展宽机制主要是自相位调制以及光波分裂等非线性效应[16]。近年来，研究者主要通过设计优化光纤结构来调控波导色散以实现全正色散特性，比如微结构光纤和拉锥光纤[20-24]。与微结构光纤相比，拉锥光纤结构相对简单，仅通过减小光纤直径就可以灵活控制其色散特性，同时也可有效提高光纤非线性系数。目前，基于全正色散拉锥硫系光纤的 SC 输出相继被报道。Al-Kadry 等[23]采用 1550 nm 波长、590 fs 脉宽的超短脉冲泵浦 3 mm 长的全正色散拉锥硫系光纤（锥腰直径为 0.58 μm），获得了 0.96～2.5 μm 波段的 SC 输出。Wang 等[25]将硫系光纤拉锥至直径为 27 μm 以实现全正色散，并用 3.25 μm 波长的飞秒激光泵浦，产生的 SC 输出

收稿日期：2021-08-27；**修回日期**：2021-09-26；**录用日期**：2021-09-30

基金项目：国家自然科学基金（62090064，61875094）、宁波大学王宽诚幸福基金

通信作者：daishixun@nbu.edu.cn

覆盖了 1.4～7.2 μm 波段。另外，Zhang 等[24]为了拓宽 SC 带宽，采用了 Te 基拉锥光纤并将直径拉至 60 μm；采用 5.5 μm 波长的飞秒脉冲泵浦获得了 1.7～12.4 μm 波段的 SC 输出。但由于自相位调制和光波分裂效应对光谱的展宽作用有限，并且泵浦功率在拉锥光纤锥区的损失较大，因此很难实现更宽的相干中红外 SC 输出。

另外，在 S 基、Se 基和 Te 基三种体系的硫系玻璃中，Te 基玻璃具有最高的非线性系数和最长的红外透过截止波长。相对 S 基和 Se 基硫系光纤，Te 基硫系光纤更适用于产生覆盖中红外以及远红外波段的 SC 输出。Jayasuriya 等[26]制备出具有较低传输损耗(在 5 ～11 μm 波段传输损耗<2 dB/m)的 Ge-As-Se-Te/Ge-As-Se 单包层阶跃型光纤(SIF)，采用中心波长为 4.65 μm、重复频率为 20.88 MHz 的飞秒脉冲泵浦 16 cm 长的光纤，获得了 2.1～11.5 μm 的 SC 输出。Jiao 等[27]制备出 Ge-As-Se-Te 组分的双包层光纤(DCF)并在其中获得了 3.2～12.1 μm 的宽带 SC 输出。但是 Te 元素的引入往往也会将硫系光纤的零色散点红移至 9 μm 以上。为了获得高相干度的宽带 SC 输出，需要对 Te 基硫系光纤色散进行调控。

本文拉制了纤芯、内包层、外包层直径比为 1∶3∶9的 Ge-As-Se-Te 双包层拉锥硫系光纤，当锥腰纤芯直径小于 12 μm 时，可实现全正色散特性。采用中心波长为 6 μm 的超短脉冲激光泵浦 10 cm 长的拉锥光纤，获得了 1.5～14.3 μm 的 SC 输出，理论计算验证了其具有高的相干特性。

2 实验与结果分析

2.1 双包层拉锥 Ge-As-Se-Te 光纤制备

本文采用的双包层硫系光纤的纤芯材料为 $Ge_{15}As_{25}Se_{40}Te_{20}$ 玻璃，内包层和外包层材料分别为 $Ge_{15}As_{25}Se_{45}Te_{15}$ 和 $Ge_{15}As_{25}Se_{50}Te_{10}$ 玻璃。首先通过动态蒸馏法将高纯的 Ge、As、Se 以及 Te 原料进行进一步提纯以去除其中的 O_2、H_2O 和 CO_2 分子杂质，并通过熔融淬冷法制备出纤芯和包层玻璃[28]。三种玻璃的线性折射率如图 1(a)所示。然后采用两步挤压法制备了双包层硫系光纤预制棒，纤芯、内包层、外包层直径比为 1∶3∶9，并在拉丝塔中将其拉制为纤芯直径为 90 μm 的光纤。为了防止光纤表面在高温下氧化导致光纤损耗增加，在预制棒挤压和光纤拉丝过程中均采用高纯氮气进行保护，并在光纤表面涂覆了 20 μm 厚的聚醚砜(PES)以增强其机械强度。为了方便对比，还制备了以 $Ge_{15}As_{25}Se_{40}Te_{20}$ 玻璃为纤芯、$Ge_{15}As_{25}Se_{45}Te_{15}$ 玻璃为包层的单包层光纤，该光纤的纤芯直径也为 90 μm，纤芯包层直径比为 1∶3。采用截断法测量了两种光纤的损耗，结果如图 1(b)所示。单包层光纤的最低损耗约为 2 dB/m，双包层光纤由于进行了预制棒的二次挤压，其整体损耗略高于单包层光纤。4.5，4.9，6.2，7.9 μm 处的吸收峰分别对应于 Se—H、Ge—H、H_2O 和 Ge—O 的杂质吸收带。

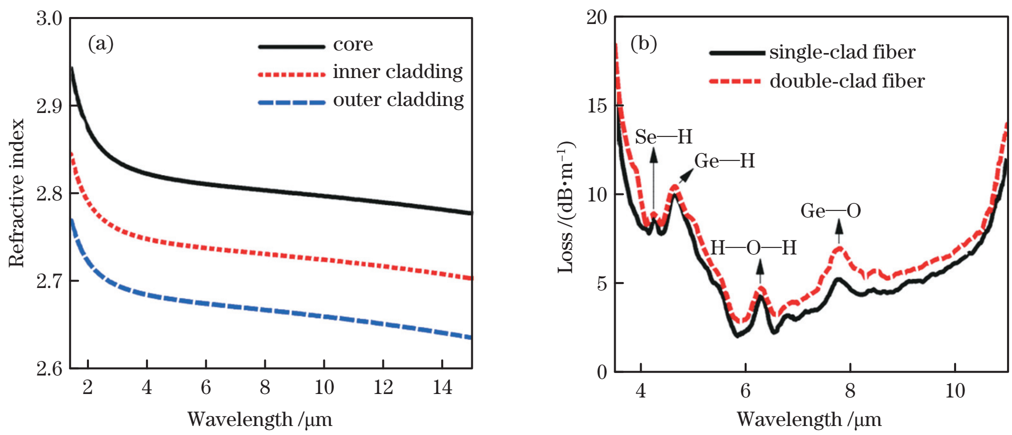

图 1 基质玻璃折射率及光纤损耗。(a)纤芯以及内外包层玻璃的折射率；(b) 双包层和单包层光纤的损耗

Fig. 1 Refractive indices of glass hosts and fiber transmission loss. (a) Refractive indices of fiber core, inner cladding glass, and outer cladding glass; (b) loss of single-clad and double clad fibers

随后采用自行搭建的拉锥平台分别拉锥单包层和双包层光纤。通过调节拉锥平台的加热区长度和拉锥速度，可以对拉锥光纤的结构参量进行精确的控制[29]。图 2(a)展示了双包层拉锥光纤的结构，图 2(b)为光纤横截面及其折射率分布图，其中 n_1、n_2 以及 n_3 分别为纤芯、内包层以及外包层玻璃的折射率。

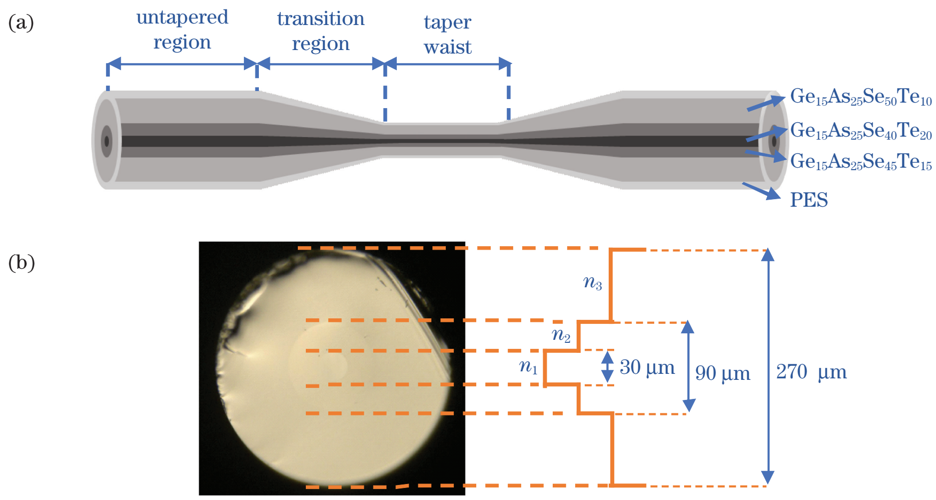

图 2 双包层拉锥硫系光纤结构及折射率分布示意图。(a)双包层拉锥硫系光纤示意图；(b)双包层硫系光纤的横截面及其折射率分布

Fig. 2 Structure and refractive index profile of double-clad chalcogenide fiber taper. (a) Schematic of double-clad chalcogenide fiber taper; (b) cross-section and refractive index profile of double-clad chalcogenide fiber

2.2 双包层拉锥 Ge-As-Se-Te 光纤的色散特性分析

根据光纤的纤芯和包层折射率数据，采用 Mode Solutions 软件数值仿真了双包层光纤的基模色散随光纤纤芯直径的变化曲线，如图 3 所示，未拉锥的双包层光纤的零色散波长位于 8.6 μm 处。随着拉锥光纤锥腰位置的纤芯直径(d)从 30 μm 减小至 14 μm，拉锥光纤的零色散波长蓝移并且出现了双零色散点。当锥腰纤芯直径小于 12 μm(锥腰外径约为 108 μm)时，光纤呈现全正色散特性。而单包层拉锥硫系光纤为了呈现全正色散，则锥腰纤芯直径需小于 10 μm(如图 3 虚线所示)，此时锥腰外径仅为 30 μm。与仅几十 μm 直径的单包层拉锥光纤相比，双包层拉锥光纤在实际操作中的机械强度更具优势，而泵浦波长处的深度正色散将会限制光纤中产生的 SC 光谱的宽度并且增强其不对称性[21]，因此，在 SC 谱产生实验中我们选用锥腰纤芯直径为 12 μm 的双包层拉锥光纤作为 SC 产生的非线性介质。

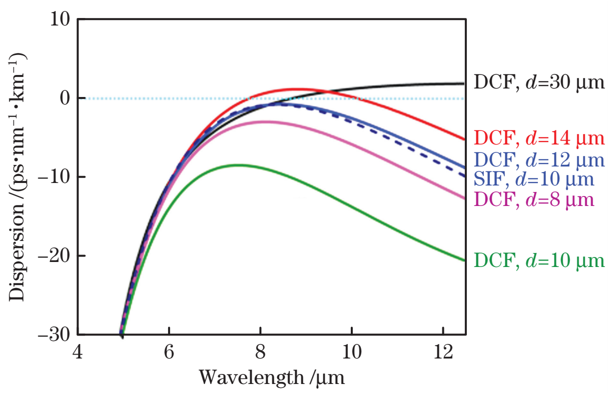

图 3 双包层(实线)和单包层(虚线)拉锥光纤的基模色散特性曲线

Fig. 3 Fundamental mode dispersion characteristic curves of double-clad (solid) and single-clad (dashed) fiber tapers

2.3 超宽中红外 SC 输出特性

用于 SC 产生的光参量放大器(OPA)泵浦脉冲的脉宽为 150 fs，重复频率为 1 kHz。为了实现 SC 带宽的最大化，首先采用了三种不同的泵浦波长去抽运 10 cm 长的双包层拉锥光纤，即 4，5，6 μm 波长，其分别对应的泵浦平均功率为 25，22，20 mW。由于双包层拉锥光纤具有全正色散的特性，因此自相位调制效应以及自陡和三阶色散引起的光波破碎效应在超短脉冲展宽的过程中起了主要作用。获得的 SC 输出结果(−30 dB 动态范围)如图 4(虚线)所示，可以看到，当泵浦波长为 4 μm 时，产生的 SC 覆盖了 1.4～12.3 μm 波段。随着泵浦波长的增大，SC 带宽也逐渐增大。当泵浦波长为 6 μm 时，可以获得覆盖 1.5～14.3 μm 的宽带 SC 输出。三种泵浦波长下的 SC 输出均呈现明显的非对称特性，一方面是因为长波段的色散斜率要小于短波段，另一方面是因为长波段的光纤损耗整体上也要小于短波段。图 4 中位于 4.5，6.2，7.9 μm 处的光谱凹陷主要是光纤中的 Se—H、H_2O 以及 Ge—O 杂质吸收造成的。因此，从光谱带宽来看，6 μm 波长处的超短脉冲更加适合作为泵浦源抽运双包层拉锥光纤。另外，我们也采用了同样的泵浦条件抽运 10 cm 长的单包层阶跃型拉锥光纤(T-SIF，锥腰纤芯直径为 10 μm)，结果如图 4 实线所示，在三种泵浦波长下获得的 SC 输出均窄于双包层拉锥光纤(T-DCF)。

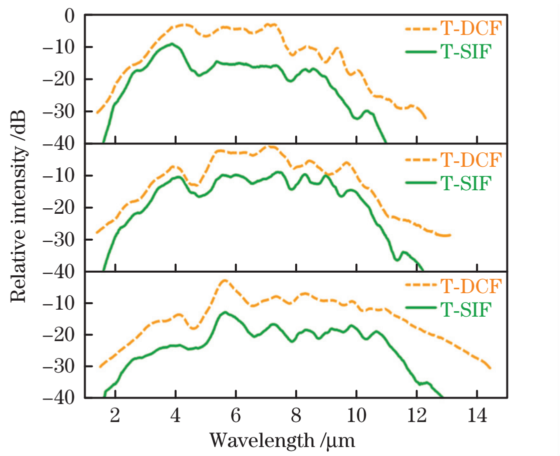

图 4 不同波长的超短激光脉冲泵浦双包层(虚线)和单包层(实线)拉锥光纤产生的 SC 输出。(a) 4 μm; (b) 5 μm; (c) 6 μm

Fig. 4 SC spectra generated from double-clad (dashed) and single-clad (solid) fiber tapers pumped by ultrashort laser pulses with different wavelengths. (a) 4 μm; (b) 5 μm; (c) 6 μm

另外,我们也采用了同样的泵浦条件抽运 10 cm 长的单包层拉锥光纤(锥腰纤芯直径为 10 μm),结果如图 4 实线所示,在三种泵浦波长下获得的 SC 输出均窄于双包层拉锥光纤。双包层的光纤结构不仅提升了拉锥光纤的机械强度,也一定程度上降低了光功率在锥区和锥腰的损失,使光谱展宽更加充分。

拉锥光纤的锥区长度也会影响所产生的 SC 特性。图 5 为同样纤芯直径、不同锥区长度(L_t)的双包层拉锥光纤中的 SC 结果。可以明显地看到,当锥区长度由 6.5 mm 逐渐增大到 9.8 mm 时,测得的 SC 展宽范围从 1.8～13 μm 增加到 1.5～14.3 μm,并且随着锥区长度的增加,光谱在长波长方向的展宽更充分,而在短波长方向的展宽不明显。对于长度和直径均相同的拉锥光纤,其非线性效应的强度是相同的,但在不同过渡区长度下,其 SC 展宽范围却不同,原因是不同过渡区长度造成的功率损耗是不相同的。当过渡区长度较短时,锥区直径变化较快,光脉冲在传输过程中具有较多的高阶模式。相反,当过渡区长度较大时,锥区直径变化较缓慢,光传输的高阶模较少,此时光传输功率较高,有利于 SC 向长波红外方向展宽[25]。另外,对比实验研究了在相同泵浦条件下未拉锥双包层光纤的 SC 输出特性。由于未拉锥光纤具有较大的有效模场面积和较小的非线性系数(与双包层拉锥光纤相比),其 SC 展宽范围仅为 1.9～11.2 μm。

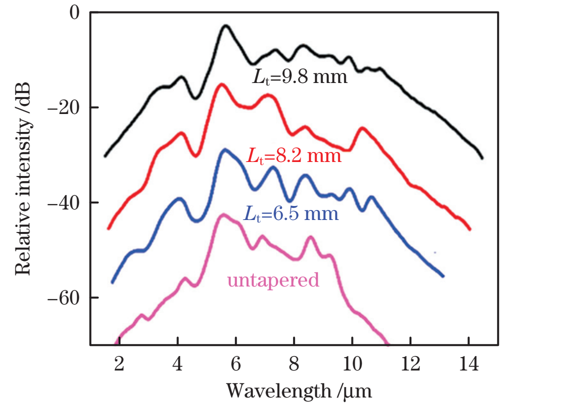

图 5 不同锥区长度下双包层拉锥光纤的 SC 输出

Fig. 5 SC spectra generated from double-clad fiber tapers with different transition region lengths

2.4 SC 相干性

SC 光谱的相干性[30]通常表示为

$$|g_{12}^{(1)}(\lambda, t_1 - t_2)| = \left| \frac{\langle E_1^*(\lambda, t_1) E_2(\lambda, t_2) \rangle}{\sqrt{\langle |E_1(\lambda, t_1)|^2 \rangle \langle |E_2(\lambda, t_2)|^2 \rangle}} \right|, \tag{1}$$

式中:$g_{12}^{(1)}$ 为光谱各波长成分的复相干度;λ 为波长;E_1 和 E_2 分别表示两次在不同随机噪声下产生的 SC 电场强度;E_1^* 为 E_1 的共轭;t_1、t_2 分别为两次 SC 光谱的获取时间,由于只考虑每个波长处 SC 的相干性,因此设 $t_1 - t_2 = 0$;$\langle \cdot \rangle$表示取平均。$g_{12}^{(1)}$ 反映的是大量计算结果的统计平均,该值的范围为 0～1,越接近 1 说明 SC 的相干性越好。

为了验证双包层拉锥光纤的 SC 输出相干特性,采用(1)式对 SC 相干性进行了计算。在计算过程中,模拟了多组带有不同入射脉冲随机噪声和自发拉曼噪声的 SC 输出,并在计算过程中考虑到了光纤损耗的影响。SC 谱模拟结果及其相干性如图 6 所示。

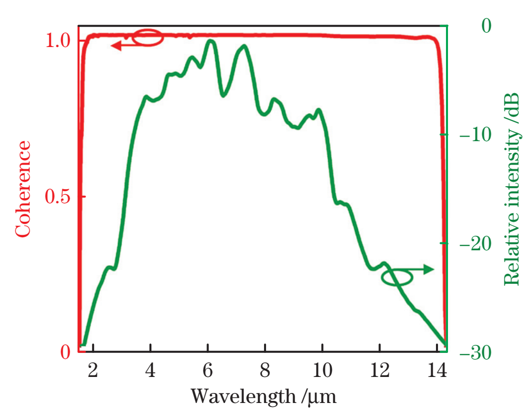

图 6 双包层拉锥光纤中的 SC 谱仿真结果及其相干特性曲线

Fig. 6 Simulated SC spectrum and its coherence property curve in double-clad fiber taper

可以看出,在 1.8～14 μm 波段范围内,一阶相干因子的值大致为 1,且相干性曲线没有明显凹陷。由于该 SC 在产生过程中均处于正常色散波段,没有受到调制不稳定性和孤子效应的影响,仅发生了自相位调制和光波分裂等非线性效应,光纤传输中伴随的噪声没有得到放大,因此光脉冲在整个传播过程中始终保持单个脉冲特性,SC 具有较好的相干性。

3 结 论

制备了具有全正色散特性的双包层拉锥 Ge-As-Se-Te 光纤中的宽带相干 SC 产生。采用波长为 6 μm 的超短脉冲激光泵浦长度为 10 cm、锥腰纤芯直径为 12 μm 以及锥区长度为 9.8 mm 的拉锥光纤,获得了 1.5～14.3 μm 的宽带 SC 输出。模拟计算结果表明,该 SC 具有高的相干性,可用于光学相干层析成像以及高精密频率测量等对光学精度和分辨率要求较高的应用领域。

参 考 文 献

[1] Petersen C R, Prtljaga N, Farries M, et al. Mid-infrared multispectral tissue imaging using a chalcogenide fiber supercontinuum source[J]. Optics Letters, 2018, 43(5): 999-1002.

[2] Ringsted T, Siesler H W, Engelsen S B. Monitoring the staling of wheat bread using 2D MIR-NIR correlation spectroscopy [J]. Journal of Cereal Science, 2017, 75: 92-99.

[3] Amiot C, Ryczkowski P, Aalto A, et al. Multi-component gas detection in the mid-IR [J]. SPIE Newsroom, 2015: 1.

[4] Kumar M, Islam M N, Terry F L, et al. Stand-off detection of solid targets with diffuse reflection spectroscopy using a high-power mid-infrared supercontinuum source[J]. Applied Optics, 2012, 51 (15): 2794-2807.

[5] Domachuk P, Wolchover N A, Cronin-Golomb M, et al. Over 4000 nm bandwidth of mid-IR supercontinuum generation in sub-centimeter segments of highly nonlinear tellurite PCFs [J]. Optics Express, 2008, 16 (10): 7161-7168.

[6] Liao M S, Gao W Q, Duan Z C, et al. Supercontinuum generation in short tellurite microstructured fibers pumped by a quasi-cw laser [J]. Optics Letters, 2012, 37(11): 2127-2129.

[7] Jia Z X, Yao C F, Li Z R, et al. Progress on novel high power mid-infrared fiber laser materials and supercontinuum laser[J]. Chinese Journal of Lasers, 2019, 46(5): 0508006.
贾志旭, 姚传飞, 李真睿, 等. 新型高功率中红外光纤激光材料与超连续谱激光研究进展[J]. 中国激光, 2019, 46(5): 0508006.

[8] Wang F, Wang K, Yao C, et al. Tapered fluorotellurite microstructured fibers for broadband supercontinuum generation[J]. Optics Letters, 2016, 41(3): 634-637.

[9] Qin G S, Yan X, Kito C, et al. Ultrabroadband supercontinuum generation from ultraviolet to 6.28 μm in a fluoride fiber[J]. Applied Physics Letters, 2009, 95(16): 161103.

[10] Dai S X, Wang Y Y, Peng X F, et al. A review of mid-infrared supercontinuum generation in chalcogenide glass fibers[J]. Applied Sciences, 2018, 8(5): 707.

[11] Wang Y Y, Dai S X. Mid-infrared supercontinuum generation in chalcogenide glass fibers: a brief review [J]. PhotoniX, 2021, 2(1): 1-23.

[12] Dai S X, Wang M, Wang Y Y, et al. Review of mid-infrared supercontinuum spectrum generation based on chalcogenide glass fibers[J]. Laser & Optoelectronics Progress, 2020, 57(7): 071603.
戴世勋, 王敏, 王莹莹, 等. 基于硫系玻璃光纤的中红外超连续谱产生研究进展[J]. 激光与光电子学进展, 2020, 57(7): 071603.

[13] Petersen C R, Møller U, Kubat I, et al. Mid-infrared supercontinuum covering the 1.4–13.3 μm molecular fingerprint region using ultra-high NA chalcogenide step-index fibre[J]. Nature Photonics, 2014, 8(11): 830-834.

[14] Ou H, Dai S, Zhang P, et al. Ultrabroad supercontinuum generated from a highly nonlinear Ge-Sb-Se fiber[J]. Optics Letters, 2016, 41(14): 3201-3204.

[15] Petersen C R, Engelsholm R D, Markos C, et al. Increased mid-infrared supercontinuum bandwidth and average power by tapering large-mode-area chalcogenide photonic crystal fibers [J]. Optics Express, 2017, 25(13): 15336-15348.

[16] Agrawal G P. Nonlinear fiber optics [M]. 5th ed. Amsterdam: Elsevier, 2013.

[17] Rao D S S, Jensen M, Grüner-Nielsen L, et al. Shot-noise limited, supercontinuum-based optical coherence tomography[J]. Light: Science & Applications, 2021, 10: 133.

[18] Zhang J, Cai Y R, Huang Q Q, et al. Near-infrared comb spectroscopy technology based on flat coherent supercontinuum [J]. Chinese Journal of Lasers, 2021, 48(7): 0711003.
张静, 蔡玉汝, 黄勤清, 等. 基于平坦相干超连续谱

的近红外光梳光谱技术[J]. 中国激光, 2021, 48(7): 0711003.
[19] Huang C L, Liao M S, Bi W J, et al. Ultraflat, broadband, and highly coherent supercontinuum generation in all-solid microstructured optical fibers with all-normal dispersion[J]. Photonics Research, 2018, 6(6): 601-608.
[20] Heidt A M, Hartung A, Bosman G W, et al. Coherent octave spanning near-infrared and visible supercontinuum generation in all-normal dispersion photonic crystal fibers[J]. Optics Express, 2011, 19(4): 3775-3787.
[21] Hooper L E, Mosley P J, Muir A C, et al. Coherent supercontinuum generation in photonic crystal fiber with all-normal group velocity dispersion[J]. Optics Express, 2011, 19(6): 4902-4907.
[22] Diouf M, Salem A B, Cherif R, et al. Super-flat coherent supercontinuum source in $As_{38.8}Se_{61.2}$ chalcogenide photonic crystal fiber with all-normal dispersion engineering at a very low input energy[J]. Applied Optics, 2017, 56(2): 163-169.
[23] Al-Kadry A, Li L, El Amraoui M, et al. Broadband supercontinuum generation in all-normal dispersion chalcogenide microwires[J]. Optics Letters, 2015, 40(20): 4687-4690.
[24] Zhang N, Peng X, Wang Y, et al. Ultrabroadband and coherent mid-infrared supercontinuum generation in Te-based chalcogenide tapered fiber with all-normal dispersion[J]. Optics Express, 2019, 27(7): 10311-10319.
[25] Wang Y Y, Dai S X, Li G T, et al. 1.4–7.2 μm broadband supercontinuum generation in an As-S chalcogenide tapered fiber pumped in the normal dispersion regime[J]. Optics Letters, 2017, 42(17): 3458-3461.
[26] Jayasuriya D, Petersen C R, Furniss D, et al. Mid-IR supercontinuum generation in birefringent, low loss, ultra-high numerical aperture Ge-As-Se-Te chalcogenide step-index fiber[J]. Optical Materials Express, 2019, 9(6): 2617-2629.
[27] Jiao K, Yao J M, Zhao Z M, et al. Mid-infrared flattened supercontinuum generation in all-normal dispersion tellurium chalcogenide fiber[J]. Optics Express, 2019, 27(3): 2036-2043.
[28] Sun Y, Dai S, Zhang P, et al. Fabrication and characterization of multimaterial chalcogenide glass fiber tapers with high numerical apertures[J]. Optics Express, 2015, 23(18): 23472-23483.
[29] Luo B H, Wang Y Y, Sun Y N, et al. Fabrication and characterization of bare Ge-Sb-Se chalcogenide glass fiber taper[J]. Infrared Physics & Technology, 2017, 80: 105-111.
[30] Liu L, Nagasaka K, Qin G S, et al. Coherence property of mid-infrared supercontinuum generation in tapered chalcogenide fibers with different structures[J]. Applied Physics Letters, 2016, 108(1): 011101.

Broadband and Coherent Supercontinuum Generation in All-Normal-Dispersion Double-Clad Ge-As-Se-Te Fiber Taper

Wang Yingying[1], Zhang Nan[2], Zhang Peiqing[1,3,4,5], Wang Xunsi[1,3,4,5], Dai Shixun[1,3,4,5*]

[1] *Laboratory of Infrared Material and Devices, The Research Institute of Advanced Technologies, Ningbo University, Ningbo, Zhejiang* 315211, *China*;
[2] *College of Electronic Science and Engineering, Nanjing University, Nanjing, Jiangsu* 210093, *China;*
[3] *Key Laboratory of Photoelectric Materials and Devices of Zhejiang Province, Ningbo, Zhejiang* 315211, *China*;
[4] *Engineering Research Center for Advanced Infrared Photoelectric Materials and Devices of Zhejiang Provinces, Ningbo, Zhejiang* 315211, *China*;
[5] *International Science & Technology Cooperation Base of Infrared Materials and Devices of Zhejiang Provinces, Ningbo, Zhejiang* 315211, *China*

Abstract

Objective Supercontinuum (SC) sources with spatial coherence, broad bandwidth, and high brightness have received considerable attention due to their significant potential in various applications, such as sensing, biomedical science, and spectral tissue imaging. In particular, the mid-infrared (MIR) spectral region is regarded as an important topic because most molecules exhibit fundamental vibrational absorption bands in this region and leave distinctive spectral fingerprints. Chalcogenide (ChG) glass has a comparatively wide transparency window (over 20 μm) and high optical nonlinearity (up to a thousand times greater than that of silica glass), making them as excellent candidates for MIR SC generation. Using fiber tapers with all-normal dispersion (ANDi) is an effective method to generate a broadband SC spectrum with high coherence in ChG fibers. However, extremely small diameters of a few micron of the tapered step-index fiber result in an energy loss in the transition region and a very low mechanical strength during preparation, optical testing and practical applications. To improve the mechanical strength and enhance the nonlinearity of the fiber, double-clad fiber tapers can be considered, which can achieve an ANDi characteristic by adding one clad layer.

Methods The ChG double-clad fiber (DCF) used in this work is made of $Ge_{15}As_{25}Se_{40}Te_{20}$ core glass, $Ge_{15}As_{25}Se_{45}Te_{15}$ inner cladding glass, and $Ge_{15}As_{25}Se_{50}Te_{10}$ outer cladding glass. High-purity materials are purified to remove oxygen, water, and carbon by dynamical distillation, and three glass rods (core size of 9 mm × 15 mm, inner cladding size of 26 mm × 15 mm, and outer cladding size of 26 mm × 15 mm) are prepared using the melt-quenching method. The linear refractive indices of the cladding glass and core glasses (Fig. 1(a)) are measured using an IR ellipsometer. The preform Ⅰ (ratio of core diameter to cladding diameter is 1∶3) and preform Ⅱ (ratio of core glass diameter to inner and outer cladding diameters is 1∶3∶9) are obtained by isolated stacked extrusion machine and then drawn into a step-index fiber (SIF) (cladding diameter of 270 μm, and core diameter of 90 μm) and a DCF (outer cladding diameter of 270 μm, inner cladding diameter of 90 μm, and outer cladding diameter of 30 μm), respectively. A polyethersulfone (PES) jacket is used to improve fiber mechanical robustness. Transmission losses of the SIF and DCF in the 3.5–11 μm range are measured via the cut back method by FTIR (Fig. 1(b)). Next, the SIF and DCF are both drawn by a homemade tapering platform. The schematic of the tapered DCF (T-DCF) (Fig. 2 (a)) and the cross-sectional image of the DCF (Fig. 2 (b)) are shown. The fundamental mode dispersion characteristic curves (Fig. 3) of the tapered double-clad fiber (T-DCF, solid) and the tapered step-index fiber (T-SIF, dashed) are calculated with the change of the core diameter. The pump pulse used for SC generation from an optical parametric amplifier (OPA) system has a pulse duration of ~150 fs and a repetition rate of 1 kHz.

Results and Discussions In order to maximize the spectral bandwidth, different pump wavelengths of 4, 5, 6 μm in the normal dispersion regime under the maximum average pump powers (25, 22, 20 mW) are used, respectively. The dependence of the resulting SC spectrum (Fig. 4) of 10 cm long ANDi T-DCF at -30 dB is measured under different pump wavelengths. During the broadening process, SPM plays an important role in the initial stage, which results in optical wave breaking due to self-steepening and third-order dispersion, leading to a significant blue- and red-shift of the spectrum. The widest SC spectrum spanning from 1.5 μm to 14.3 μm is obtained when pumped at 6 μm. For comparison, the SC broadening in an ANDi T-SIF (with 10 μm waist core diameter) with the same length as T-DCF is also measured under the same pumping conditions. In fact, the double clad leads not only to improve the mechanical strength but also lower the energy loss in the transition region of the tapered fiber for SC generation, which leads to wide SC generation. In addition, the dependence of the resulting SC spectra on transition region length (L_t) at the same core diameter of 12 μm is also measured (Fig. 5). When the value of L_t is increased from 6.5 mm to 9.8 mm, the measured spectral bandwidth of SC shows a tendency to increase both in blue side and red side. Because a large L_t makes the diameter of the transition region change slowly, it is always accompanied by a low number of high-order modes and low power consumption, leading to a wider SC spectrum in T-DCF. The maximum broadening of SC generation in a T-DCF and the corresponding spectral coherence property are calculated (Fig. 6), confirming that the SC spectrum shows a highly coherent property.

Conclusions In summary, an ultrabroadband SC spanning from 1.5 μm to 14.3 μm with a high coherent property is obtained in a 10 cm long ANDi T-DCF pumped at 6 μm. For comparison, the SC broadening in an ANDi T-SIF under the same pumping conditions is also measured. Our results show that double clad leads not only to improve the mechanical strength but also lower the energy loss in the transition region of the fiber taper for ultra-broadband SC generation, which has a considerable practical potential in various applications.

Key words laser optics; nonlinear optics; fiber fabrication; supercontinuum generation; fiber optics